In vivo directed evolution of an ultrafast Rubisco from a semianaerobic environment imparts oxygen resistance

Julie L. McDonald[a,b] (ID), Nathan P. Shapiro[a], Amanuella A. Mengiste[a], Sarah Kaines[c] (ID), Spencer M. Whitney[c] (ID), Robert H. Wilson[a,1], and Matthew D. Shoulders[a,d,e,1] (ID)

Carbon dioxide (CO_2) assimilation by the enzyme Ribulose-1,5-bisphosphate Carboxylase/Oxygenase (Rubisco) underpins biomass accumulation in photosynthetic bacteria and eukaryotes. Despite its pivotal role, Rubisco has a slow carboxylation rate ($k_{cat}^{CO_2}$) and is competitively inhibited by oxygen (O_2). These traits impose limitations on photosynthetic efficiency, making Rubisco a compelling target for improvement. Interest in Form II Rubisco from *Gallionellaceae* bacteria, which comprise a dimer or hexamer of large subunits, arises from their nearly fivefold higher $k_{cat}^{CO_2}$ than the average Rubisco enzyme. As well as having a fast $k_{cat}^{CO_2}$ (25.8 s^{-1} at 25 °C), we show that *Gallionellaceae* Rubisco (GWS1B) is extremely sensitive to O_2 inhibition, consistent with its evolution under semianaerobic environments. We therefore used an in vivo mutagenesis-mediated screening pipeline to evolve GWS1B over six rounds under oxygenic selection, identifying three catalytic point mutants with improved ambient carboxylation efficiency: Thr-29-Ala (T29A), Glu-40-Lys (E40K), and Arg-337-Cys (R337C). Full kinetic characterization showed that each substitution enhanced the CO_2 affinity of GWS1B under oxygenic conditions by subduing oxygen affinity, leading to 25% (E40K), 11% (T29A), and 8% (R337C) enhancements in carboxylation efficiency under ambient O_2 at 25 °C. By contrast, under the near anaerobic natural environment of *Gallionellaceae*, the carboxylation efficiency of each mutant was impaired ~16%. These findings demonstrate the efficacy of artificial directed evolution to access distinctive regions of catalytic space in Rubisco.

Ribulose-1,5-bisphosphate Carboxylase/Oxygenase (Rubisco) | carbon fixation | directed evolution | enzyme engineering | MutaT7

The enzyme Ribulose-1,5-bisphosphate Carboxylase/Oxygenase (Rubisco) is essential for life on Earth, fixing atmospheric carbon dioxide (CO_2) to organic carbon during photosynthesis (1). The Rubisco enzyme family has diverse isoforms across phylogeny. Plants, algae, and many mixotrophic and autotrophic bacteria utilize Form I Rubisco, where the enzyme is composed of a large (RbcL) and small (RbcS) subunit as an $RbcL_8RbcS_8$ hexadecamer. Form II and Form III Rubisco, found in bacteria and archaea, lack RbcS and present as arrangements of RbcL dimers ($RbcL_2$–$RbcL_{10}$) (2–4). Form II/III Rubisco display lower substrate specificity for CO_2 over oxygen (O_2; $S_{C/O}$) than Form I enzymes, a deficiency attributed to their lack of RbcS (5).

Despite their widespread prevalence in Nature and essentiality for carbon fixation, Rubisco enzymes display striking inefficiencies. The rate of Rubisco carboxylation is most often in the range of 1 to 10 reactions per second (6)—much slower than most other enzymes involved in carbon metabolism. The enzyme also reacts promiscuously with O_2, producing 2-phosphoglycolate (2-PG) that must be recycled via energy-consuming mechanisms, including photorespiration in plants (7) and the phosphoglycolate salvage pathway in bacteria (8). Rubisco's weak specificity for CO_2 may be related to the evolutionary emergence of its complex, 5-step, catalytic mechanism in an anoxic atmosphere, prior to the rise of oxygenic photosynthesis (9, 10). The emergence of Earth's current O_2-rich atmosphere has necessitated Rubisco to gain selectivity for CO_2 over O_2, albeit at a profoundly slow pace (11). Kinetic trends across the Rubisco family suggest that improvements in $S_{C/O}$ come at the expense of $k_{cat}^{CO_2}$ (6, 12, 13), in particular for Form II Rubisco whose particularly high $k_{cat}^{CO_2}$ values (>10 s^{-1}) and low $S_{C/O}$ (<20 mol/mol) (2) are associated with environments high in dissolved CO_2 and/or low in O_2, such as acidic iron-rich soils (14) and the deep sea (15).

A large body of both theoretical and experimental research indicates that improving the efficiency of Rubisco carboxylation can enhance plant photosynthesis (1, 16–20),

Significance

Given Rubisco's crucial role in carbon dioxide assimilation, addressing its slow carboxylation rate and oxygen inhibition is a significant challenge. Utilizing one of the fastest known, yet also highly oxygen-sensitive, Rubisco—from the bacteria *Gallionellaceae*—we applied an in vivo directed evolution pipeline in *Escherichia coli* to identify substitutions that specifically enhance carboxylation efficiency under ambient oxygen, a condition distinct from *Gallionellaceae's* natural semianaerobic environment. Our findings underscore the potential of directed evolution to unlock catalytic capabilities for Rubisco, with implications for both fundamental research and practical agricultural applications.

Author affiliations: [a]Department of Chemistry, Massachusetts Institute of Technology, Cambridge, MA 02139; [b]Department of Biology, Massachusetts Institute of Technology, Cambridge, MA 02139; [c]Plant Science Division, Research School of Biology, The Australian National University, Canberra, ACT 0200, Australia; [d]Broad Institute of Massachusetts Institute of Technology and Harvard, Cambridge, MA 02139; and [e]Koch Institute for Integrative Cancer Research at Massachusetts Institute of Technology, Cambridge, MA 02139

making Rubisco itself a promising engineering target to enhance crop productivity and yields. Photosynthetic modeling in crops like rice, wheat, and soybean shows such improvements require combined improvements in the $k_{cat}^{CO_2}$, CO_2-affinity ($K_M^{CO_2}$) and $S_{C/O}$ of Rubisco within the aerobic chloroplast environment (16, 19). While several directed evolution studies on nonplant Rubisco have identified mutations that improve $k_{cat}^{CO_2}$ (21–26), anaerobic $K_M^{CO_2}$ (21, 25, 27–31), and $S_{C/O}$ (21–23) of Rubisco, in most instances, they overlook how the enzyme's sensitivity to O_2 is impacted (21, 24–30, 32–34). This knowledge is critical to ascertaining the biologically relevant aerobic $K_M^{CO_2}$ (21% O_2) and carboxylation efficiency [$k_{cat}^{CO_2}/K_M^{CO_2}$ (21% O_2)] values needed to simulate Rubisco performance in an oxygenic photosynthesis environment (17, 19).

In addition to Rubisco engineering efforts, several studies have sought to profile the natural catalytic landscape of the Rubisco family (2, 35, 36). Form II Rubisco enzymes from the semianaerobic bacterial family *Gallionellaceae* have garnered attention from such profiling efforts and from metagenomic analyses (2, 37), as they display some of the fastest Rubisco-mediated carboxylation rates ever measured (15 to 29 s^{-1}) (2, 38, 39). Interestingly, *Gallionellaceae* Rubisco, while very fast, also undesirably have very high affinities for O_2 (38). The combination of these extreme and unique properties (fast carboxylation kinetics and high sensitivity to O_2) position *Gallionellaceae* Rubisco as an advantageous starting point for directed evolution, with the potential to uncover distinct loci important for mitigating the enzyme's reactivity with O_2.

Here, we describe an in vivo laboratory-directed evolution pipeline for Rubisco that leverages the targeted mutagenesis tool MutaT7 (40–47). This method sidesteps the low-throughput, shallow, and labor-intensive in vitro mutagenesis approaches employed in prior Rubisco directed evolution campaigns (21–29, 31–34, 48). MutaT7 is a targeted, genome-encoded mutagen composed of a deaminase fused to a T7 RNA polymerase (T7 RNAP). MutaT7 processively and selectively mutates any DNA region that is flanked by a T7 promoter and terminator. The high mutagenesis frequency (40–47) of MutaT7 positions it as a useful tool for deep sampling of the Rubisco sequence landscape. We apply MutaT7 (42) in tandem with Rubisco-dependent *Escherichia coli* (RDE/RDE2) (23) to evolve a hexameric *Gallionellaceae* Rubisco (termed GWS1B, PDBID: 5C2G) originating from a groundwater sample (37). Our campaign converged on multiple "winner" mutants encoding amino acid substitutions positioned near the active site and oligomeric interfaces. Consistent with the aerobic selection pressure we applied, kinetic analysis revealed that some of the mutations imparted O_2 resistance on GWS1B variants that also retained their other beneficial catalytic features, thereby enhancing aerobic carboxylation efficiencies.

In sum, by beginning our evolution campaign with an exceptionally fast but also remarkably O_2-sensitive natural Rubisco, we were able to uncover Rubisco variants that exist in a distinctive region of catalytic space for Rubisco. These results strongly motivate continued Rubisco engineering efforts that can improve the enzyme beyond its natural capabilities.

Results

Biochemical Characterization of GWS1B Rubisco.
Kinetic characterization of both wild-type and C-terminal polyhistidine-tagged GWS1B showed that the epitope tag did not impact $k_{cat}^{CO_2}$ (25.8 s^{-1}; Fig. 1*A*) or $K_M^{CO_2}$ (161 to 165 μM) (Dataset S1),

allowing use of immobilized metal affinity chromatography-purifiable C-terminally tagged GWS1B for further work. These GWS1B hexamer (RbcL$_6$) carboxylation properties are similar to dimeric *Gallionella* sp. Rubisco (RbcL$_2$; $k_{cat}^{CO_2}$ = 27.5 s^{-1}) (2, 39), despite their RbcL sharing only 68% primary sequence identity (Dataset S1). Both of these *Gallionella* Rubisco isoforms are approximately twofold faster than the model *Rhodospirillum rubrum* Form II Rubisco (Fig. 1*A*), and share a common affinity for CO_2 (149 to 165 μM) and $S_{C/O}$ (9 mol/mol; Dataset S1). The exceptionally fast GWS1B does, however, display a heightened O_2 sensitivity ($K_M^{O_2}$ = 98 μM) relative to *R. rubrum* Rubisco ($K_M^{O_2}$ = 159 μM). This increased sensitivity to O_2 causes the carboxylation efficiency of GWS1B under anaerobic versus ambient O_2 conditions to differ by 73%, compared to a 62% difference for *R. rubrum* Rubisco (Fig. 1*B*) (30, 37, 38, 48). These findings emphasize how high Rubisco CO_2 fixation rates can be achieved via multiple evolutionary routes (i.e., are not limited to an isolated region of sequence space) with varying impact on the enzymes' affinity and specificity for CO_2 and O_2.

Alongside GWS1B's extreme CO_2 fixation rate and O_2 sensitivity, GWS1B displays a remarkably high solubility upon expression in *E. coli* (~77% of the total expressed RbcL; Fig. 1*C*). This property could provide a compelling advantage for directed evolution in RDE when aiming to select for kinetic, rather than solubility, enhancing mutants. In prior RDE studies with cyanobacterial Rubisco, where 80 to 99% of translated RbcL monomers form insoluble aggregates, the majority of higher fitness-conferring RbcL variants identified were those that enhanced RbcL folding and assembly into soluble RbcL$_8$RbcS$_8$ complexes (21, 23, 25, 27–29, 31–33). Thus, we anticipated that the high solubility of GWS1B would be particularly advantageous, as it would bias selection toward improvements in Rubisco carboxylation kinetics rather than solubility. Moreover, we expected that the high levels of soluble GWS1B expression from the single-copy number bacterial artificial chromosome (BAC) vectors used in MutaT7-driven in vivo directed evolution campaigns would be beneficial for successful RDE selection from a single-copy vector (46).

In Vivo Directed Evolution of GWS1B Rubisco using MutaT7-RDE.
Conventional Rubisco-directed evolution campaigns rely on gene diversification by error-prone (ep)-PCR, followed by library screening using RDE or *rbcL* null photosynthetic hosts (Fig. 1*D*, conventional approach) (21–29, 31–33, 48). These campaigns, while occasionally successful in identifying higher carboxylase activity Rubisco catalytic mutants, have suffered from low-mutagenic throughput, owing to the labor-intensive process of ep-PCR-mediated library creation, colony-picking, and analysis. We developed a Rubisco evolutionary pipeline combining MutaT7 with RDE and next-generation sequencing (NGS) to create an in vivo Rubisco mutagenesis system suited to repeated rounds of directed evolution in quick progression. Our system utilizes MutaT7-Dual8, a DH10B-derived *E. coli* strain that contains two genomically encoded mutagenic T7 RNAP fusions that install transition mutations at loci between a T7 RNAP promoter and terminator sequence (42) (Fig. 1*D*). MutaT7-Dual8 was transformed with the plasmid pACYC$^{prk:nptII}$, enabling arabinose-tunable expression of a phosphoribulokinase–neomycin phosphotransferase fusion (PRK-NPTII) that both phosphorylates the endogenous metabolite ribulose-5-phosphate into ribulose-1,5-bisphosphate (RuBP, the sugar substrate of Rubisco) and confers kanamycin resistance. As RuBP is a foreign and toxic metabolite to *E. coli*, cell survival can be made dependent
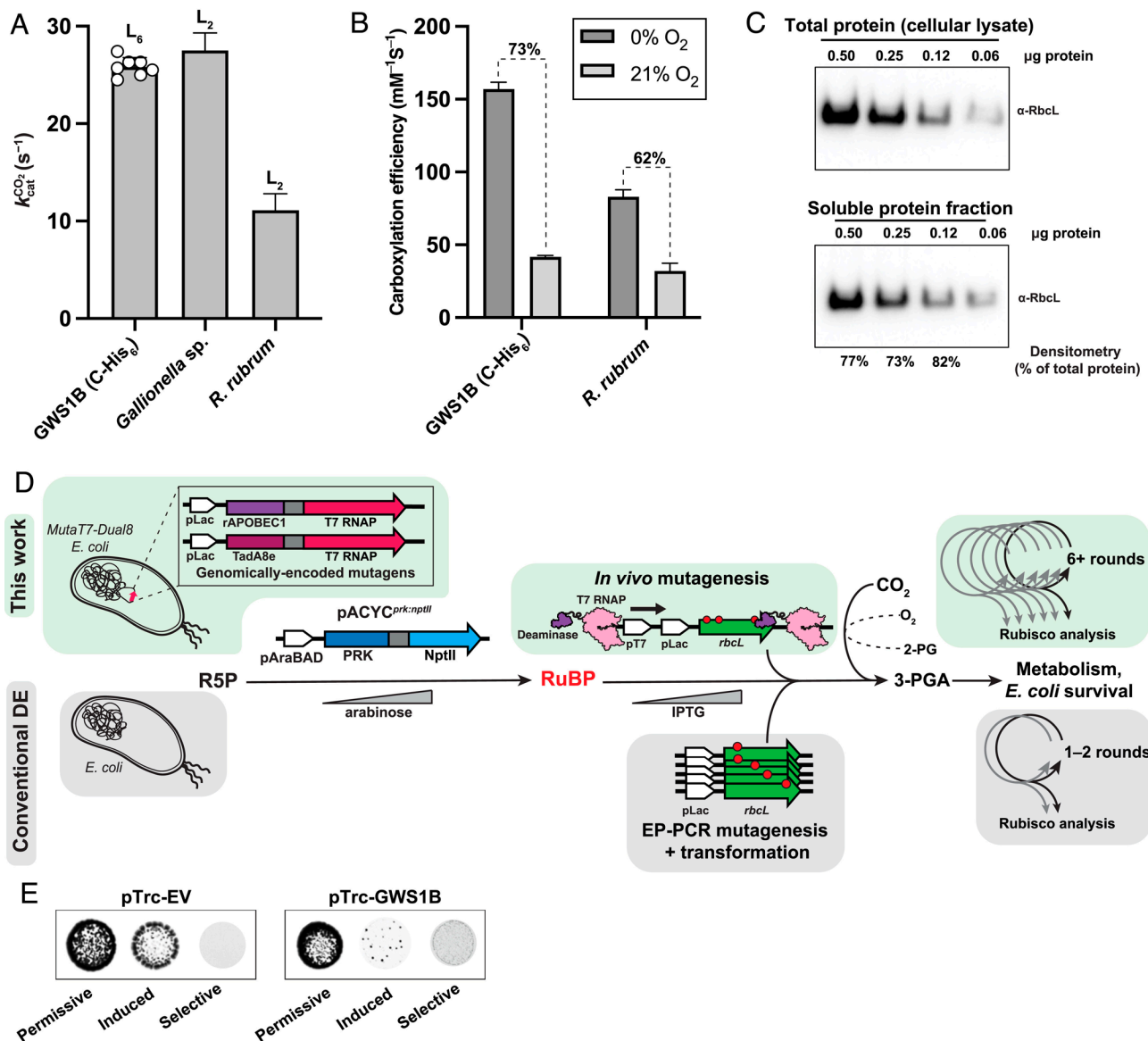
Fig. 1. Biochemistry of GWS1B Rubisco and potential for in vivo directed evolution in *Escherichia coli*. (*A*) Carboxylation rates for C-terminally tagged GWS1B Rubisco (this work), as well as for *Gallionella* sp. Rubisco (2) and *Rhodospirillum rubrum* Rubisco (48). (*B*) Carboxylation efficiencies at 0% O_2 and 21% O_2 for GWS1B and *R. rubrum* Rubisco (48). (*C*) Western blot analysis of Rubisco levels detected in total protein lysate (top) compared to the soluble protein fraction (bottom) when GWS1B is expressed from the pTrc-GWS1B plasmid, revealing the very high soluble expression of GWS1B. (*D*) Traditional Rubisco-directed evolution workflow versus targeted mutagenesis-mediated in vivo directed evolution workflow. In vivo directed evolution is mediated by in-cell, MutaT7-based mutagenesis rather than by extracellular, error-prone PCR (ep-PCR) mutagenesis followed by transformation into *E. coli* cells. MutaT7-based mutagenesis, enabled by a deaminase-T7 RNA polymerase (T7 RNAP) fusion binding to and processing from the T7 RNAP promoter site (pT7) on *rbcL*, generates high levels of downstream mutations in the plasmid DNA and avoids the need for step-wise generation of mutations and transformation, endowing deeper mutagenesis and more rapid progress between rounds of directed evolution. In both workflows, an exogenous *prk* gene is expressed to create a circuit where *E. coli* survival is dependent on Rubisco-catalyzed carboxylation and detoxification of RuBP. R5P = Ribulose-5-phosphate; RuBP = Ribulose-1,5-bisphosphate; 2-PG = 2-phosphoglycolate; 3-PGA = 3-phosphoglycerate. (*E*) RDE testing of GWS1B against an empty vector (pTrc-EV) control. Permissive growth media contains no additives, induced growth media contains 0.5 mM IPTG for expression of Rubisco, and selective growth media contains 0.5 mM IPTG, kanamycin at 400 mg/mL, and 0.15% ʟ-arabinose for expression of PRK-NPTII.

on Rubisco-mediated RuBP clearance (23, 33, 48). Such RDE screens include selection on kanamycin to avoid the growth of any false positives arising from mutations in pACYC$^{prk:nptII}$ that might impair PRK, and hence toxic RuBP, production (Fig. 1*D*).

As observed previously, the production of Rubisco in *E. coli* can itself impair cell viability (30, 49). Indeed, high-level expression of GWS1B in DH10B impairs colony growth (Fig. 1*E*, "induced"). Still, in pACYC$^{prk:nptII}$ transformed DH10B (here termed DH10B-RDE selection) we observed that cell growth was dependent on GWS1B expression under 0.15% w/v arabinose PRK-NPTII induction (Fig. 1*E*, "selective"). These findings confirmed the suitability of GWS1B for RDE-mediated selection of

mutants that enhance cell fitness during PRK-NPTII induction. We thus transformed MutaT7-Dual8 containing pACYC$^{prk:nptII}$ with a MutaT7-targeting BAC vector encoding polyhistidine-tagged GWS1B (BAC-GWS1B). We named this mutagenesis-selection system, containing all the necessary components for in vivo directed evolution of Rubisco, MutaT7-RDE (Fig. 1*D*, this work).

Within just 30 d, BAC-GWS1B was subjected to six rounds of evolution in MutaT7-RDE under incremental increases in arabinose-induced PRK-NPTII selection pressure (Fig. 2*A*). Each round consisted of a 24 h MutaT7-induced continual mutagenesis period in liquid culture, before plating on selective media and incubating in air supplemented with 10% v/v CO_2 for three days.
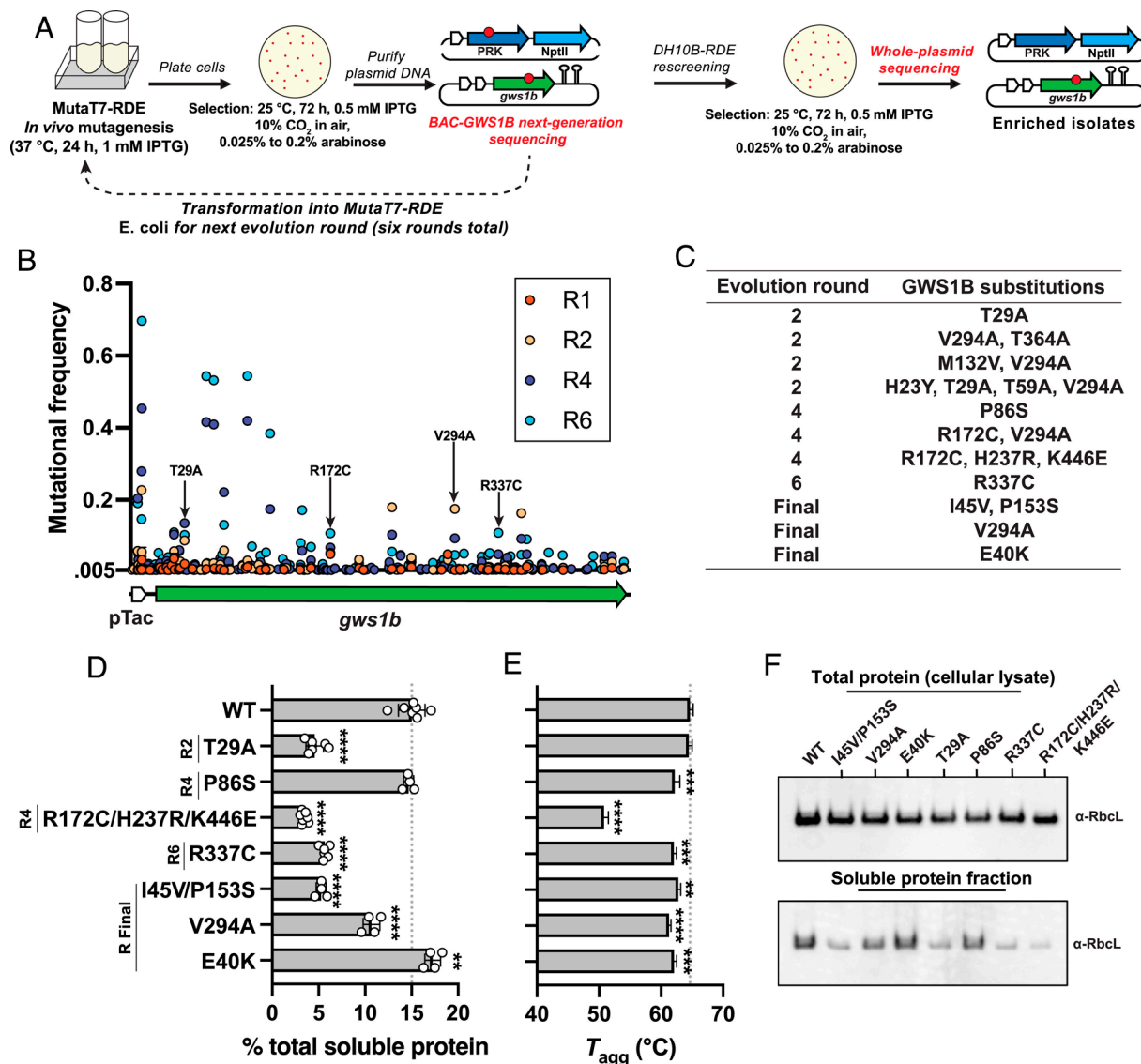
Fig. 2. Identification and biochemical characterization of GWS1B variants. (*A*) Schematic of MutaT7-RDE workflow. (*B*) Map of the promoter and GWS1B-coding region of the BAC evolution plasmid showing mutational frequency at the DNA base level during sequenced rounds of evolution. Nonsynonymous mutations from clonal isolates are indicated with arrows. (*C*) Nonsynonymous mutations found in clonal isolates of GWS1B in rounds 1, 2, 4, 6, and final rescreening round of evolution. (*D*) Soluble, folded Rubisco content of selected variants in *E. coli* quantified by [^{14}C]-CABP binding (50). Data are the means and SD of three replicates with significance shown relative to wild-type GWS1B as analyzed by one-way ANOVA. **$P \leq 0.005$; ***$P \leq 0.0005$; ****$P \leq 0.0001$. (*E*) Aggregation temperature (T_{agg}) of selected variants. Significance testing and labels are consistent with (*D*). (*F*) SDS-PAGE immunoblots of GWS1B RbcL levels in the soluble and total protein fractions upon expression of GWS1B variants in *E. coli*.

The resulting *E. coli* colonies were harvested and the BAC-GWS1B and pACYC$^{prk:nptII}$ plasmids were isolated for short read next-generation sequencing (NGS). The copurified plasmids were also *Sfi*I-digested (cutting only pACYC$^{prk:nptII}$) and the BAC-GWS1B plasmids retransformed into either fresh MutaT7-RDE cells for the next round of MutaT7-RDE selection, or into DH10B-RDE for rescreening and whole-plasmid sequencing of any faster-growing "winner" clonal isolates (Fig. 2*A*).

The short-read NGS data revealed that the high-frequency (above detection threshold) mutations that accrued in BAC-GWS1B during MutaT7-RDE selection were highly enriched between the T7 promoter and terminator regions (Fig. 2*B* and *SI Appendix*, Fig. S1) (42), including in the tac promoter sequence driving GWS1B expression (*SI Appendix*, Table S1). As expected, transition mutations accounted for all nonsynonymous mutations in the *gws1b* gene. Encouragingly, mutational frequencies at over 20 specific sites in *gws1b* showed substantial variation between

evolutionary rounds two and four and generally continued to enrich with increasing selection pressure into the sixth and final DH10B-RDE selection round (Dataset S2). Comparative sequence alignment of GWS1B with other members of the Rubisco family (*SI Appendix*, Fig. S2) showed that the selected GWS1B mutations occurred in poorly conserved regions that plausibly are more tolerant to mutational change, and hence are more readily accessible during MutaT7-RDE selection.

Whole-plasmid sequencing from DH10B-RDE rescreened clonal isolates following evolution rounds 2, 4, and 6 identified multiple nonsynonymous mutations in *gws1b* (Fig. 2*C*). In addition, many synonymous mutations in *gws1b* and mutations in the promoter and plasmid replication elements were detected (*SI Appendix*, Table S1). Whether these extraneous mutations influenced DH10B-RDE fitness through artifactual impacts on GWS1B expression or BAC-GWS1B copy number remains untested. We focused our attention instead on 11 *gws1b* mutant genes identified

via isolate screening (Fig. 2*C*), with each cloned into a clean pTrc backbone to avoid any vector mutation artifacts, expressed in DH10B *E. coli*, and then purified for biochemical analysis.

Evaluating the Speed, Solubility, and Stability of GWS1B Rubisco Variants. Initial comparisons of relative carboxylase activities measured via spectrophotometry (2, 50) indicated that five of the purified mutant GWS1B enzymes shared wild-type-like carboxylation rates, three had 2 to 10-fold lower rates and three displayed little or no measurable activity (*SI Appendix*, Fig. S3). It remains unclear how the three apparently inactive variants supported growth during DH10B-RDE rescreening, and could even relate to a loss of activity during the purification process. We do note, however, that directed evolution campaigns, including RDE-based selection campaigns, often encounter false positives (24, 26, 33, 49)—for example, owing to plasmid instability (33) or transposon insertion in *prk* (22, 23, 49). Fusion of PRK to NPTII should eliminate false positives owing to transposon insertion or plasmid instability, but does not protect against ablation of PRK function via a point mutation. Indeed, several point mutations in pACYC*prk:nptII* were identified by NGS in each round of MutaT7-RDE selection (*SI Appendix*, Fig. S4). Some of these mutations may reduce or destroy the ribulose-5-phosphate phosphorylation activity of PRK-NPTII while maintaining kanamycin resistance. The acquisition of comparable mutations in pACYC*prk:nptII* during DH10B-RDE rescreening may have allowed growth of some escape mutants even with reduced GWS1B Rubisco function.

We proceeded with the six GWS1B variants that displayed wild-type or better carboxylation activity (*SI Appendix*, Fig. S3). We first sought to assess whether these variants were selected due to improved GWS1B solubility, rather than improved kinetic features. We quantified the percentage of soluble, folded GWS1B relative to total cellular protein using a ^{14}C-2-Carboxyarabinitol-1,5-bisphosphate (^{14}C-CABP) binding assay (50). This assay revealed that the P86S and E40K GWS1B variants, selected in the fourth and final selection rounds, respectively, shared wild-type levels of GWS1B production in DH10B *E. coli*. All three enzymes accumulated to ~15% w/w of the soluble cellular protein (Fig. 2*D*). By contrast, the other variants displayed 20 to 80% reductions in soluble, folded GWS1B production, despite the temperature of aggregation (T_{agg}) for all of these variants appearing to retain near wild-type levels of stability (Fig. 2*E*). Moreover, all six successfully formed the RbcL$_6$ holoenzyme as assessed using native PAGE (*SI Appendix*, Fig. S5). We also evaluated the lower-activity triple mutant GWS1B R172C/H237R/K446E using these methods. There was noticeable precipitation of this variant during purification—possibly explaining the inability of the initial spectrophotometric assays to detect activity (*SI Appendix*, Fig. S3). We indeed observed that the triple mutant led to poor production of soluble GWS1B and lowered the T_{agg} > 10 °C in vitro, likely limiting the amount of RbcL$_6$ complexes detectable by ^{14}C-CABP binding (Fig. 2 *D* and *E*).

Additional SDS-PAGE and immunoblotting analyses showed that, while wild-type equivalent levels of each GWS1B RbcL variant were translated in DH10B *E. coli* (lysate sample; Fig. 2*F*), the proportion of produced GWS1B that was soluble in the cytosol differed between the variants (soluble sample; Fig. 2*F*). Notably, the relative levels of soluble RbcL detected by blotting correlated well with the proportion of functional enzyme quantified by ^{14}C-CABP binding (Fig. 2*D*), suggesting that the soluble RbcL detected accurately reflects the fraction stably assembled as a functional RbcL$_6$ holoenzyme. In sum, while none of the selected GWS1B variants had any discernable impact on GWS1B RbcL translation, the majority of substitutions quite substantially limited the folding and assembly of RbcL$_6$ holoenzyme. Together,

these observations indicated the GWS1B variants selected in our platform did not arise from increases in solubility, thus motivating their kinetic evaluation.

Comprehensive Kinetic Evaluation of Evolved GWS1B Rubisco Variants. We performed a full kinetic analysis of the GWS1B variants T29A, P86S, R337C, I45V/P153S, V294A, and E40K, as well as the triple mutant R172C/H237R/K446E using radiometric carboxylation activity assays (Fig. 3 *A–G* and Dataset S3). The carboxylation rate of all variants remained similar to or decreased relative to wild-type GWS1B (Fig. 3*A*), consistent with the spectrophotometric estimate of carboxylation rate (*SI Appendix*, Fig. S3). This result was expected, owing to the already extremely high carboxylation rate of wild-type GWS1B that limits selection pressure on this parameter. $K_M^{CO_2}$ measured at 0% O$_2$ increased for all but one variant (P86S; Fig. 3*B*). $S_{C/O}$ remained comparable or slightly decreased relative to wild-type GWS1B (Fig. 3*C*).

Critically, however, $K_M^{CO_2}$ at 0% O$_2$ is an irrelevant parameter in the context of aerobic RDE selection. That is, we evolved the normally near-anaerobic GWS1B enzyme under the unnatural selection pressure of ambient O$_2$ concentrations with the hypothesis that GWS1B variants with improved fitness would show gains in resistance to O$_2$ inhibition. To test this hypothesis, we derived the apparent K_M for O$_2$ ($K_M^{O_2}$) for each GWS1B variant (Fig. 3*D* and *SI Appendix*, Fig. S6). In almost all instances, the selected variants reduced the sensitivity of GWS1B to O$_2$ inhibition (i.e., the variants increased $K_M^{O_2}$), with only V294A increasing the enzyme's apparent affinity for O$_2$ (Fig. 3*D*). Upon accounting for these changes in O$_2$ affinity, the $K_M^{CO_2}$ under ambient oxygen [$K_M^{CO_2}(21\% \ O_2)$] for each enzyme showed that all the selected variants, except V294A, had higher than wild-type aerobic affinities for CO$_2$ (Fig. 3*E* and Dataset S3).

Taken together, these data reveal that while the anaerobic carboxylation efficiencies of each evolved GWS1B variant do not exceed wild-type (Fig. 3*F*), under atmospheric O$_2$ the carboxylation efficiency of the T29A, R337C, and E40K GWS1B variants are improved 11, 8, and 25%, respectively (Fig. 3*G*). The consequence is that, relative to wild-type GWS1B, these three selected variants can support higher rates of CO$_2$ fixation in ambient O$_2$ environments (Fig. 3*H*; solid lines) but not in an anaerobic setting (Fig. 3*H*; dashed lines). Particularly noteworthy is the broad CO$_2$ range under which the identified substitutions would benefit GWS1B aerobic catalysis, with even the weaker performing R337C substitution supporting faster than wild-type carboxylation rates up to ~500 μM CO$_2$ (Fig. 3*H*), a concentration equivalent to that naturally achievable in cyanobacterial carboxysomes during CO$_2$-concentrating mechanism (CCM) induction (51).

It is unclear how the V294A, I45V/P153S, and R172C/H237R/K446E variants were selected given their impaired kinetic fitness. While in terms of altered affinities for CO$_2$ and O$_2$, the triple mutant showed the greatest improvement [247% higher $K_M^{O_2}$; 33% lower $K_M^{CO_2}(21\% \ O_2)$], its twofold lower $k_{cat}^{CO_2}$ impaired aerobic carboxylation efficiency by 23% relative to wild-type GWS1B (Dataset S3). Considering the cellular toxicity associated with GWS1B production in *E. coli* (Fig. 1*E*), one possibility is that the lower solubility of these three variants (Fig. 2 *D* and *F*), may somehow have provided a fitness advantage that improved MutaT7-RDE and DH10B-RDE growth during selection. Indeed, *E. coli* expressing GWS1B V294A or I45V/P153S grew more quickly than *E. coli* expressing wild-type GWS1B (*SI Appendix*, Fig. S7).
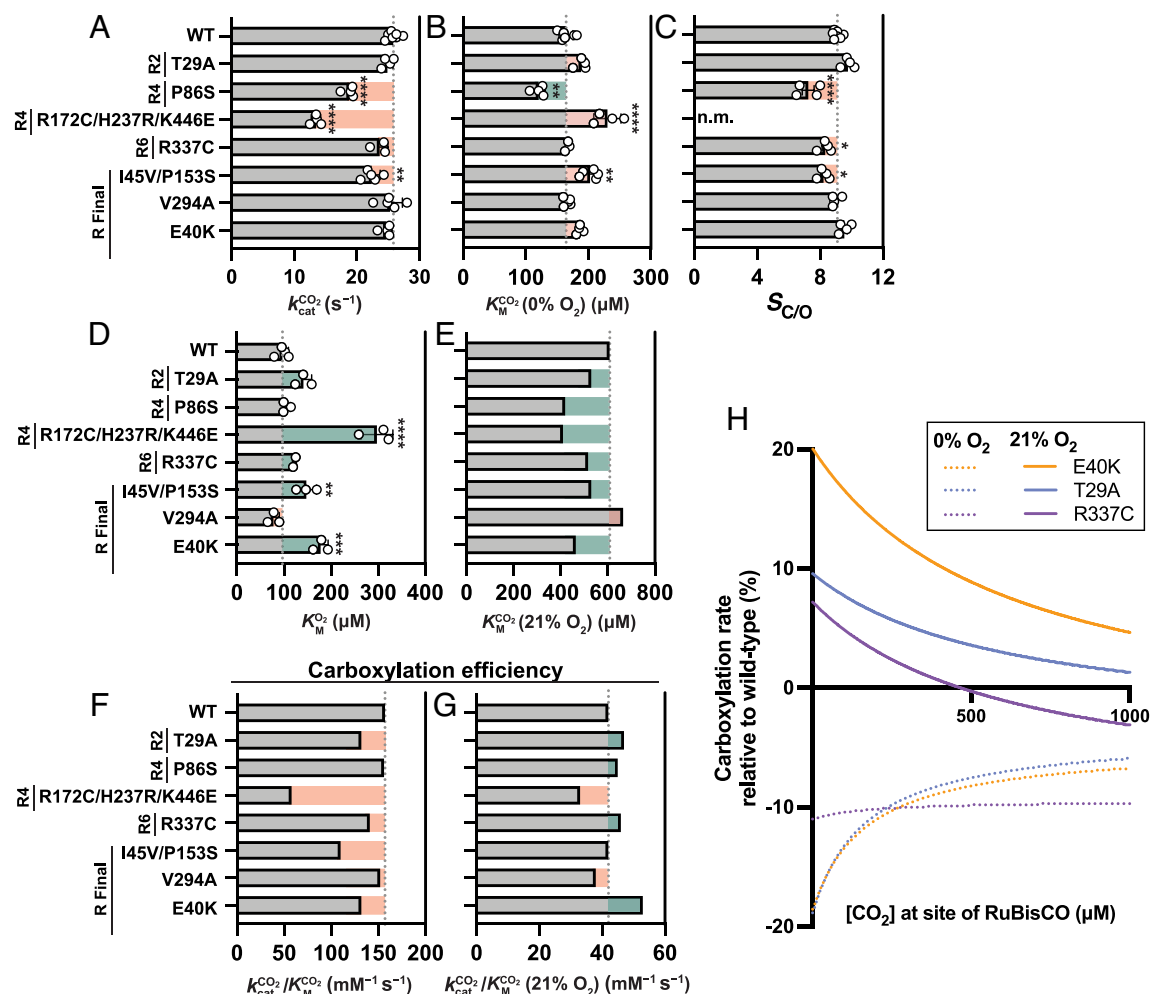
Fig. 3. Kinetic characterization of GWS1B variants. (*A*) Carboxylation rate. (*B*) Affinity for CO_2. (*C*) Specificity factor. (*D*) Affinity for O_2. Asterisks indicate *p*-value as calculated by one-way ANOVA followed by a post hoc Tukey test. *$P \leq 0.05$; **$P \leq 0.005$; ***$P \leq 0.0005$; ****$P \leq 0.0001$. (*E*) Affinity for CO_2 in air. (*F*) Carboxylation efficiency at 0% O_2. (*G*) Carboxylation efficiency at 21% O_2. (*H*) Carboxylation rates of GWS1B E40K, GWS1B T29A, and GWS1B R337C relative to wild-type GWS1B at 0% or 21% O_2 as a function of CO_2 concentration.

Selected Substitutions in GWS1B Cluster Near the Active Site and at Protein–Protein Interfaces. Structural analysis of the carboxylase-enhanced GWS1B variants shows the N-domain substitution T29A is located 20 Å away from the active site behind an α-helix, with N-domain E40K 15.4 Å away from the active site (Fig. 4*A*). The C-domain R337C substitution is located very far from any active site on the surface distal to both dimer and hexamer interfaces (Fig. 4*B*).

Similarly to E40K, whose position near the active site also positions it near the RbcL–RbcL interface, the solubility-influencing substitutions P86S, R172C, H237R, V294A, and K446E all locate to the RbcL–RbcL interface (Fig. 4*B*), and P153S lies at the interface between adjoining RbcL$_2$ dimers (Fig. 4*C*). These observations suggest the observed solubility impediments may not arise from changes in chaperonin-assisted folding of the GWS1B RbcL monomers, but rather that the amino acid substitutions at the surface of the RbcL–RbcL interface impede RbcL$_2$ and RbcL$_6$ oligomeric assembly. The kinetics of these variants show that the substitutions inflict long-range structural rearrangements on the active site architecture that, in most instances, unwantedly impaired catalytic performance (Dataset S3).

Mapping the location of the selected GWS1B RbcL substitutions revealed that they typically colocated to the respective functional region (active site or interface) of the model Form II *R. rubrum* Rubisco and model Form I plant *N. tabacum* Rubisco

(Dataset S4). This observation suggests substitutions at these corresponding RbcL residues may also impart favorable kinetic properties across the Rubisco family. Indeed, when compared to the *R. rubrum* Rubisco deep mutational scanning analysis of Prywes et al. (30), 50% of the selected GWS1B mutations occurred at loci where fitness was improved in *R. rubrum* Rubisco (Dataset S4). This outcome is striking when one considers that only 0.14% of substitutions in the *R. rubrum* Rubisco survey were differentiated as fitness-improving. Taken together, the improvements we observed in Rubisco catalysis in GWS1B reveal multiple pathways to O_2 resistance and support the notion that laboratory-based in vivo directed evolution can push Rubisco beyond existing natural catalytic boundaries.

Discussion

In this work, we introduce an in vivo directed evolution platform for Rubisco enzymes and use it to evolve Rubisco from *Gallionellaceae*, yielding variants with improved carboxylation efficiency and rates in air. This system builds upon years of foundational work on Rubisco evolution by accelerating the duration of evolution rounds, reducing researcher intervention, and deeply sampling Rubisco sequence space. The success of this evolution campaign is both a proof-of-concept for in vivo Rubisco-directed evolution and a demonstration of exceeding the known limits of
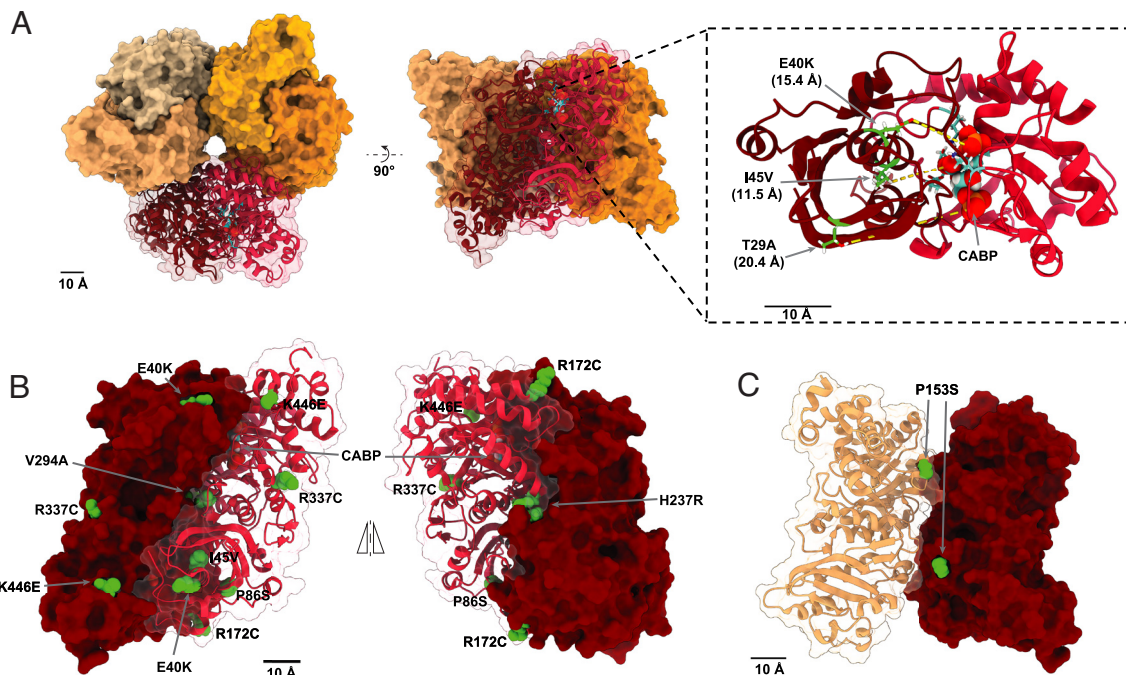
Fig. 4. Mapping evolved variants onto GWS1B. (*A*) Substitutions T29A, E40K, and I45V are positioned near the GWS1B active site. PDBID: 5C2G (37). (*B*) E40K, I45V, P86S, R172C, H237R, V294A, and K446E occur at the dimer interface. R337C is surface-exposed. (*C*) P153S occurs at the hexamer interface of GWS1B.

carboxylation capacity for a Form II Rubisco, a feat so far untenable owing to the inherently fast speed and high *E. coli* solubility exhibited by the primitive homo-oligomeric enzymes in this lineage (30, 48).

Exerting an oxygenic selection pressure on a Rubisco isoform isolated from a low-oxygen environment yielded improvements to $K_M^{CO_2}$ (21% O_2) and $K_M^{O_2}$, leading to a substantial net increase in carboxylation efficiency in air for this normally highly O_2-sensitive Rubisco. The GWS1B variants identified here demonstrate that anaerobic and ambient carboxylation efficiencies are not intrinsically linked. Thus, going forward, the effects of O_2 on Rubisco activity must be considered when undertaking any Rubisco engineering campaign to fully grasp and analyze changes in catalytic fitness, particularly for C3 plant Rubisco that contend for available CO_2 in an environment rich in dissolved O_2.

The mechanism by which the selected mutations provide O_2 resistance is not yet clear. The substitutions T29A and E40K, which enhance ambient carboxylation efficiency, are within 20 Å of the active site, possibly creating subtle structural changes that benefit the affinity for CO_2 over O_2. Seven selected substitutions that lie at either the dimer or hexamer interface of GWS1B altered $K_M^{O_2}$, though not always resulting in an increase in carboxylation efficiency in an ambient atmosphere. This observation is not the first instance of amino acid substitutions at Rubisco protein–protein interfaces affecting relative affinities for CO_2 and O_2. Selected substitutions clustered at the interface between the large and small Rubisco subunits during a previous directed evolution of the Form I *Thermosynechococcus elongatus* Rubisco, causing an increase in carboxylation efficiency in air (23). Designed structural substitutions that transition GWS1B from hexamer to dimer also impacted catalysis, increasing both $S_{C/O}$ and, to a larger extent, $K_M^{O_2}$, albeit at the cost of decreasing $k_{cat}^{CO_2}$ and carboxylation efficiency (38). A recent deep mutational scan of Form II *R. rubrum* Rubisco identified only a handful of single amino acid substitutions, all at the dimer interface, that enhanced affinity for CO_2 under anoxia,

albeit accompanied by substantial decreases in $k_{cat}^{CO_2}$ or carboxylation efficiency, and with undetermined impact on $K_M^{O_2}$ (30). Hence, there is accumulating evidence, including our work here, that residues distant from the active site at RbcL among differing Rubisco lineages have a pervasive, and sometimes beneficial, impact on catalysis. Moreover, for GWS1B, the T29A, E40K, and R337C substitutions subvert the debilitating decrease in carboxylation rate that the aforementioned variants in other Form II Rubisco suffer from, while still improving CO_2 affinity in air. They also emphasize the importance of scrutinizing how mutations impact the O_2 sensitivity of a Rubisco. In the absence of such studies, essential insight into how the enzyme's carboxylation rate under ambient O_2 is impacted by novel substitutions is lacking. As indicated above, such understanding is critical when attempting to simulate performance in an aerobic photosynthetic environment, such as a leaf.

In conclusion, we deployed an in vivo directed evolution system to expand the catalytic limits of Rubisco beyond what has been observed in nature, focusing on minimizing inhibitory oxygenation while stimulating carboxylation. Future use of MutaT7-RDE, as well as orthogonal protein engineering approaches, will continue to elucidate the Rubisco sequence–structure–function landscape. Efficient Rubisco enzymes engineered in the laboratory will provide key insights into the fundamental mechanisms of carboxylation and oxygenation and can be utilized as essential starting points to improve photosynthesis.

Materials and Methods

MutaT7-RDE Workflow. To generate the MutaT7-RDE strain, a single colony of BAC-GWS1B and pACYC*prk:nptII* transformed Dual8 *E. coli* (42) were grown on agar-solidified Luria broth (LB) containing 100 µg/mL ampicillin and 35 µg/mL chloramphenicol (LB-AC). A single colony was inoculated into 5 mL of LB-AC containing 1 mM isopropyl β-D-1-thiogalactopyranoside (IPTG) to induce MutaT7 mutagenesis. After incubating at 37 °C and 180 rpm for 24 h, a 0.1 µL aliquot of this culture was plated on LB-AC agar containing 50 µg/mL triphenyl tetrazolium

chloride (TTC; Sigma-Aldrich) to visualize colony-forming units (cfu) per volume of the culture. 250 µL aliquots of the remaining culture (~5 to 7 × 10^5 cfu) were plated on selective LB (LB-AC agar plates with 400 µg/mL kanamycin, 0.5 mM IPTG, and 50 µg/mL TTC) containing between 0.025 to 0.2% w/v L-arabinose (Sigma-Aldrich) to modulate PRK-NPTII production. L-Arabinose concentrations were incrementally increased by 0.025% w/v between rounds 1 to 4, and then increased to 0.15% w/v (round 5) and 0.2% w/v (round 6). The plates were incubated at ~25 °C in a commercial premixed high CO_2 atmosphere (10:21:69% v/v CO_2:O_2:N_2) until colony growth was observed (~72 h). The resulting colonies were harvested by scraping into 5 to 10 mL LB, centrifuged for 10 min at 5,000×g, and the BAC-GWS1B and pACYC$^{prk:nptII}$ plasmids were copurified (Wizard® *Plus* SV Miniprep kit; Promega) for NGS or further MutaT7-RDE rescreening.

For NGS, the plasmids were diluted to 20 ng/µL for Nextera DNA Flex kit (Illumina) preparation before sequencing in duplicate using a 150 paired-end kit on an Element Biosciences AVITI sequencer. For MutaT7-RDE rescreening, 1 µg of the copurified plasmids were digested with *Sfi*I (New England Biolabs) for 2 h at 50 °C, repurified (Wizard® SV PCR clean-up kit; Promega), and eluted in 15 µL H$_2$O. After electroporating 5 µL into MutaT7-RDE, the cells were recovered in 1 mL LB for 1 h at 37 °C/180 rpm before plating 1 µL on LB-AC to assess transformation efficiency and diluting the remaining cells into 4 mL LB-AC with 1 mM IPTG to initiate the next round of MutaT7 mutagenesis.

For nonmutagenic rescreening, the purified *Sfi*I-digested plasmid was electroporated into pACYC$^{prk:nptII}$-transformed DH10B (DH10B-RDE) *E. coli* and plated on selective LB containing 0.2% w/v L-arabinose and incubated at ~25 °C under 10% v/v CO$_2$ for 3 to 5 d. The fastest-growing colonies were individually grown in LB-AC, and the plasmids purified and whole-plasmid sequenced (Plasmidsaurus).

To verify variants from the later rounds of evolution, *rbcL* libraries from rounds 4 and 6 were PCR-amplified using the primers GWS1Bfor (5′-ATATCCATGGACC AAAGTAATCGTTACGCCGAC-3′) and GWS1Brev (5′-AATATGAGCTCCTATTCGCCATTC AGGCTGCGTTAATTAAACCAC-3′) and cloned as a *Nco*I-*Sac*I fragment into a pTrc vector. The fastest-growing colonies upon rescreening were picked and analyzed as variants from the "final" round of evolution.

Next-Generation Sequencing Analysis. Output fastQ files were aligned to BAC-GWS1B and pACYC$^{prk:nptII}$ using the Burrows-Wheeler Aligner (BWA) (52). Alignments were down-sampled to 10% to reduce file size, then were indexed, sorted, and a pileup file was generated using Samtools (53). Nonreference base frequencies at each position in the reference plasmid were calculated using Samtools and a custom Perl script. Mutational scatter plots were generated from these tables using Prism. Further analysis of high-percentage SNPs was completed with Geneious Prime. Mutations at 0.10% or higher frequency (determined using a read quality score of 30) in BAC-GWS1B that were present in duplicate sequencing of at least one round of evolution are listed in Dataset S2. Full scripts for NGS processing are available at https://github.com/juliemcdonald/GWS1B.

Rubisco Purification. Mutant and wild-type GWS1B *rbcL* genes were PCR-amplified using the primers GWS1Bfor and GWS1Brev, cloned as a *Nco*I-*Sac*I fragment into a pTrc vector, and transformed into DH10B *E. coli*. Large (1 L) or small (10 to 20 mL) LB containing 100 µg/mL ampicillin (LB-A) cultures were grown for Rubisco purification and high-resolution kinetic analyses, respectively. Cultures were grown at 37 °C at 180 rpm until an OD$_{600}$ of 0.6 to 0.8 was attained, before inducing GWS1B expression with 0.5 mM IPTG at 23 °C for 16 h and then centrifuging for 10 min at 8,000×g and 4 °C. Cell pellets were then snap-frozen in liquid N$_2$ for storage at −80 °C.

For Rubisco purification, the stored cell pellets were resuspended in 20 mL ice-cold buffer [20 mM HEPES, pH 8.0, 50 mM NaCl, 1 mM phenylmethylsulfonyl fluoride (PMSF; Amersco), 5 mM DL-Dithiothreitol (DTT; Sigma-Aldrich), and 1 µL of DNase (Sigma-Aldrich)] then lysed using a needle-tipped sonicator (50% amplitude with three 20 s on/off cycles) on ice. Following centrifugation (20,000×g for 20 min at 4 °C), the soluble protein was filtered through a 0.22 µm filter before immobilized metal affinity chromatography purification using a 1 mL HisPur™ Cobalt Resin (Thermo Fisher Scientific) column equilibrated with column buffer (20 mM HEPES and 50 mM NaCl at pH 8.0). After washing with 5 mL column buffer with 20 mM imidazole (Alfa Aesar), GWS1B proteins were eluted with 2 mL column buffer containing 500 mM imidazole. The eluted protein was dialyzed at 4 °C o/n against column buffer, concentrated using an Amicon®

Ultra Centrifugal Filter (Sigma-Aldrich) with a 100 kDa molecular weight cutoff, and then snap-frozen for future use. Purity and oligomeric state were evaluated using Native PAGE (*SI Appendix*, Fig. S5), and GWS1B concentration was calculated from NanoDrop 280 nm absorbance using an extinction coefficient of 63,175 M^{-1} cm^{-1} for GWS1B. Purified Rubisco were used to quantify $S_{C/O}$ using the [1-^{3}H]-RuBP consumption assay (54).

Spectrophotometric Measurement of Rubisco Activity. Carboxylation rates for each purified GWS1B enzyme were measured using the enzyme-coupled nicotinamide adenine dinucleotide (NAD$^+$/NADH) reduction spectrophotometric assay in 96-well microtiter plates, as previously described (2, 50). Purified GWS1B proteins (1 mg/mL) were activated in 100 mM EPPS-NaOH at pH 7.6 containing 10 mM MgCl$_2$ and 10 mM NaHCO$_3$ before diluting 1:500 into 0.2 mL reactions containing 10 mM MgCl$_2$ and 10 mM NaHCO$_3$ and initiating with 5 µL 20 mM RuBP (50). Assays were performed in triplicate at 30 °C, tracing the decrease in absorbance at 340 nm over 20 min at 53 s intervals. The slope of the linear decline at 340 nm over time was used to calculate the Rubisco carboxylation rate (s^{-1}) (50).

GWS1B Rubisco Content and Kinetic Characterization. Bacterial pellets were sonicated on ice (30 s at 60% amplitude) in 0.5 to 1.0 mL assay buffer (50 mM EPPS-NaOH at pH 7.8 containing 15 mM MgCl$_2$, 1 mM EDTA, 1 mM PMSF, and 5 mM DTT), then centrifuged (20,000×g for 2 min at 2 °C) and aliquots of the soluble protein were used for quantifying protein content (Pierce™ Bradford Protein Assay Kit against bovine serum albumin), Rubisco content measurements, ^{14}CO$_2$ fixation activity assays, and SDS-PAGE analyses. Samples were preactivated with 25 mM NaHCO$_3$ for 10 to 20 min at 25 °C before quantifying Rubisco content by ^{14}C-CABP binding, as previously described (50, 55). Measures of Rubisco concentration as a % (w/w) of total cell soluble protein assumed a molecular mass of 50 kDa for GWS1B RbcL. ^{14}CO$_2$-fixation assays to measure $k_{cat}^{CO_2}$, $K_M^{CO_2}$, and $K_M^{O_2}$ at 25 °C were undertaken as previously described (23), with the following additional considerations for GW1SB: Following activation of Rubisco with 20 mM NaH^{14}CO$_3$, the samples were diluted 50-fold into assays containing six incremental ^{14}CO$_2$ concentrations between 0 to 360 µM, 0 to 440 µM, or 0 to 540 µM in reactions preequilibrated with atmospheres containing 0% (anaerobic), 10%, or 20% v/v O$_2$ in N$_2$, respectively (*SI Appendix*, Fig. S6).

SDS-PAGE, Western Blotting, and Native PAGE. For SDS-PAGE and immunoblotting, samples of total cellular protein following sonication (lysate), as well as the soluble protein following centrifugation (soluble), were processed for SDS-PAGE separation through NuPAGE™ Bis-Tris Mini Protein Gels, 4 to 12% (Thermo Fisher Scientific), as previously described (23). Sample loading was normalized to soluble protein content (with matching volume of lysate loaded per sample), and the separated proteins either visualized by Coomassie staining or transferred onto nitrocellulose membranes (Hybond C, APBiotech) using an Xcell transfer cell (Novex), according to the manufacturer's specifications. Immunoblotting was performed as previously described (56), and GWS1B RbcL contents were compared by probing with an antibody to *R. rubrum* Rubisco (56). Immunoreactive GWS1B RbcL was visualized using the Clarity Western ECL substrate (Bio-Rad). The fluorescence signal was imaged and signal densitometry quantified using a ChemiDoc MP Imaging System (Bio-Rad).

For native PAGE, purified GWS1B proteins were thawed on ice and diluted to 1 µg/mL in 20 mM HEPES and 50 mM NaCl at pH 8.0. 1 µg of protein was loaded onto a Novex™ Tris-Glycine 4 to 12% Mini Protein Gel (Thermo Fisher Scientific). The gel was run in NativePAGE™ Running Buffer (Thermo Fisher Scientific) at 120 V for 2.5 h at 4 °C, then stained with Coomassie InstantBlue® Protein Stain (Abcam). 1 µg of bovine thyroglobulin (Sigma-Aldrich) and 1 µg of bovine serum albumin (Sigma-Aldrich) were used as molecular weight markers.

Growth Curves. pTrc-GWS1B plasmids were transformed into DH10B chemically competent *E. coli* (New England Biolabs). A single colony was used to inoculate 5 mL of LB-A and was incubated overnight at 37 °C and 180 rpm. This culture was used to inoculate 200 µL of LB-A to an OD of 0.005 in a 96-well plate. OD was measured at 600 nm for 16 h ± IPTG in an Agilent BioTek Synergy HTX plate reader. Data reported are means of normalized triplicate growth curves.

DH10B-RDE Spot Testing. Colonies of pTrc-GWS1B and pACYC$^{prk:nptII}$ cotransformed DH10B *E. coli* (DH10B-RDE) were grown on LB-AC containing 50 µg/mL TTC. A colony was used to inoculate 1 mL of LB-AC, which was then incubated at

37 °C and 180 rpm until an OD_{600} of ~0.2. The resulting culture was diluted with LB to an equivalent OD_{600} of 1×10^{-4} and 20 μL was spotted onto an LB-AC plate containing 50 μg/mL TTC, 0.5 mM IPTG, 400 μg/mL kanamycin, and incremental concentrations (0 to 0.3% w/v) of L-arabinose. The plates were incubated at ~25 °C in air supplemented with 2% v/v CO_2 and colony growth was monitored over 10 d.

Data, Materials, and Software Availability. Sequencing data are available at NCBI Bioproject ID PRJNA1275035 (57). Other study data are included in the article and/or supporting information. Plasmids pACYCprk:nptII (#239580), BAC-GWS1B (#239581), and pTrc-GWS1B (#239582) are on Addgene (58). MutaT7-Dual8 is available from the Belgian Coordinated Collections of Microorganisms, catalog LMBP 13434.

1. N. Prywes, N. R. Phillips, O. T. Tuck, L. E. Valentin-Alvarado, D. F. Savage, Rubisco function, evolution, and engineering. *Annu. Rev. Biochem.* **92**, 385–410 (2023).
2. D. Davidi *et al.*, Highly active rubiscos discovered by systematic interrogation of natural sequence diversity. *EMBO J.* **39**, e104081 (2020).
3. S. M. Whitney, R. L. Houtz, H. Alonso, Advancing our understanding and capacity to engineer nature's CO_2-sequestering enzyme, Rubisco. *Plant Physiol.* **155**, 27–35 (2011).
4. F. R. Tabita, S. Satagopan, T. E. Hanson, N. E. Kreel, S. S. Scott, Distinct form I, II, III, and IV Rubisco proteins from the three kingdoms of life provide clues about Rubisco evolution and structure/function relationships. *J. Exp. Bot.* **59**, 1515–1524 (2008).
5. L. Schulz *et al.*, Evolution of increased complexity and specificity at the dawn of form I Rubiscos. *Science* **378**, 155–160 (2022).
6. A. I. Flamholz *et al.*, Revisiting trade-offs between Rubisco kinetic parameters. *Biochem.* **58**, 3365–3376 (2019).
7. B. J. Walker, A. VanLoocke, C. J. Bernacchi, D. R. Ort, The costs of photorespiration to food production now and in the future. *Annu. Rev. Plant Biol.* **67**, 107–129 (2016).
8. N. J. Claassens *et al.*, Phosphoglycolate salvage in a chemolithoautotroph using the calvin cycle. *Proc. Natl. Acad. Sci. U. S. A.* **117**, 22452–22461 (2020).
9. E. G. Nisbet *et al.*, The age of Rubisco: the evolution of oxygenic photosynthesis. *Geobiol.* **5**, 311–335 (2007).
10. T. J. Erb, J. Zarzycki, A short history of RubisCO: the rise and fall (?) of Nature's predominant CO_2 fixing enzyme. *Curr. Opin. Biotechnol.* **49**, 100–107 (2018).
11. J. W. Bouvier, D. M. Emms, S. Kelly, Rubisco is evolving for improved catalytic efficiency and CO_2 assimilation in plants. *Proc. Natl. Acad. Sci. U. S. A.* **121**, e2321050121 (2024).
12. Y. Savir, E. Noor, R. Milo, T. Tlusty, Cross-species analysis traces adaptation of rubisco toward optimality in a low-dimensional landscape. *Proc. Natl. Acad. Sci. U. S. A.* **107**, 3475–3480 (2010).
13. P. M. Shih *et al.*, Biochemical characterization of predicted Precambrian RubisCO. *Nat. Commun.* **7**, 10382 (2016).
14. M. Esparza, E. Jedlicki, C. González, M. Dopson, D. S. Holmes, Effect of CO_2 concentration on uptake and assimilation of inorganic carbon in the extreme acidophile *Acidithiobacillus ferrooxidans*. *Front. Microbiol.* **10**, 603 (2019).
15. J. Zhang *et al.*, Discovery of a readily heterologously expressed Rubisco from the deep sea with potential for CO_2 capture. *Bioresour. Bioprocess.* **8**, 86 (2021).
16. R. E. Sharwood, O. Ghannoum, S. M. Whitney, Prospects for improving CO_2 fixation in C_3-crops through understanding C_4-Rubisco biogenesis and catalytic diversity. *Curr. Opin. Plant Biol.* **31**, 135–142 (2016).
17. R. E. Sharwood, Engineering chloroplasts to improve Rubisco catalysis: Prospects for translating improvements into food and fiber crops. *New Phytol.* **213**, 494–510 (2017).
18. X.-G. Zhu, D. R. Ort, M. A. J. Parry, S. von Caemmerer, A wish list for synthetic biology in photosynthesis research. *J. Exp. Bot.* **71**, 2219–2225 (2020).
19. M. Gionfriddo, T. Rhodes, S. M. Whitney, Perspectives on improving crop Rubisco by directed evolution. *Semin. Cell Dev. Biol.* **155**, 37–47 (2023).
20. K. D. Cocon, P. Luis, The potential of RuBisCO in CO_2 capture and utilization. *Prog. Energy Combust. Sci.* **105**, 101184 (2024).
21. P. Durão *et al.*, Opposing effects of folding and assembly chaperones on evolvability of Rubisco. *Nat. Chem. Biol.* **11**, 148–155 (2015).
22. R. H. Wilson, H. Alonso, S. M. Whitney, Evolving *Methanococcoides burtonii* archaeal Rubisco for improved photosynthesis and plant growth. *Sci. Rep.* **6**, 22284 (2016).
23. R. H. Wilson, E. Martin-Avila, C. Conlan, S. M. Whitney, An improved *Escherichia coli* screen for Rubisco identifies a protein–protein interface that can enhance CO_2-fixation kinetics. *J. Biol. Chem.* **293**, 18–27 (2018).
24. Y. Zhou, S. Whitney, Directed evolution of an improved Rubisco; *in vitro* analyses to decipher fact from fiction. *Int. J. Mol. Sci.* **20**, e5019 (2019).
25. D. N. Greene, S. M. Whitney, I. Matsumura, Artificially evolved *Synechococcus* PCC6301 Rubisco variants exhibit improvements in folding and catalytic efficiency. *Biochem. J.* **404**, 517–524 (2007).
26. Z. Cai, G. Liu, J. Zhang, Y. Li, Development of an activity-directed selection system enabled significant improvement of the carboxylation efficiency of Rubisco. *Prot. Cell* **5**, 552–562 (2014).
27. S. Satagopan, S. S. Scott, T. G. Smith, F. R. Tabita, A Rubisco mutant that confers growth under a normally "inhibitory" oxygen concentration. *Biochem.* **48**, 9076–9083 (2009).
28. S. Satagopan, F. R. Tabita, RubisCO selection using the vigorously aerobic and metabolically versatile bacterium *Ralstonia eutropha*. *FEBS J.* **283**, 2869–2880 (2016).
29. S. Satagopan, K. A. Huening, F. R. Tabita, Selection of cyanobacterial (*Synechococcus* sp. Strain PCC 6301) RubisCO variants with improved functional properties that confer enhanced CO_2-dependent growth of *Rhodobacter capsulatus*, a photosynthetic bacterium. *mBio* **10**, 1128 (2019).
30. N. Prywes *et al.*, A map of the Rubisco biochemical landscape. *Nature* **638**, 823–828 (2025).
31. O. Mueller-Cajar, S. M. Whitney, Evolving improved *Synechococcus* Rubisco functional expression in *Escherichia coli*. *Biochem.* **414**, 205–214 (2008).
32. S. A. Smith, F. R. Tabita, Positive and negative selection of mutant forms of prokaryotic (cyanobacterial) Ribulose-1,5-bisphosphate Carboxylase/Oxygenase. *J. Mol. Biol.* **331**, 557–569 (2003).
33. M. R. Parikh, D. N. Greene, K. K. Woods, I. Matsumura, Directed evolution of RuBisCO hypermorphs through genetic selection in engineered *E. coli*. *Protein Eng. Des. Sel.* **19**, 113–119 (2006).
34. B. J. Gomez-Fernandez *et al.*, Directed -*in vitro*- evolution of Precambrian and extant Rubiscos. *Sci. Rep.* **8**, 5532 (2018).
35. J. Galmés *et al.*, Expanding knowledge of the Rubisco kinetics variability in plant species: Environmental and evolutionary trends. *Plant Cell Environ.* **37**, 1989–2001 (2014).
36. B. de Pins *et al.*, A systematic exploration of bacterial form I rubisco maximal carboxylation rates. *EMBO J.* **43**, 3072–3083 (2024).
37. V. A. Varaljay *et al.*, Functional metagenomic selection of ribulose 1,5-bisphosphate carboxylase/oxygenase from uncultivated bacteria. *Environ. Microbiol.* **18**, 1187–1199 (2016).
38. A. K. Liu *et al.*, Structural plasticity enables evolution and innovation of RuBisCO assemblies. *Sci. Adv.* **8**, eadc9440 (2022).
39. Y.-C.C. Tsai, Z. Guo, R. Milo, O. Mueller-Cajar, Updated values for Table 1 of fastest rubisco carboxylation rates in Davidi *et al.* 2020. *EMBO J.* **44**, 2397–2399 (2025).
40. B. Álvarez, M. Mencía, V. de Lorenzo, L. Á. Fernández, *In vivo* diversification of target genomic sites using processive base deaminase fusions blocked by dCas9. *Nat. Commun.* **11**, 6436 (2020).
41. H. Park, S. Kim, Gene-specific mutagenesis enables rapid continuous evolution of enzymes *in vivo*. *Nucleic Acids Res.* **49**, e32 (2021).
42. A. A. Mengiste *et al.*, Expanded Mutat7 toolkit efficiently and simultaneously accesses all possible transition mutations in bacteria. *Nucleic Acids Res.* **51**, e31 (2023).
43. D. Seo, B. Koh, G.-E. Eom, H. W. Kim, S. Kim, A dual gene-specific mutator system installs all transition mutations at similar frequencies *in vivo*. *Nucleic Acids Res.* **51**, e59 (2023).
44. A. A. Mengiste *et al.*, MutaT7^{GDE}: A single chimera for the targeted, balanced, efficient, and processive installation of all possible transition mutations *in vivo*. *ACS Synth. Biol.* **13**, 2693–2701 (2024).
45. C. L. Moore, L. J. Papa, M. D. Shoulders, A processive protein chimera introduces mutations across defined DNA regions in vivo. *J. Am. Chem. Soc.* **140**, 11560–11564 (2018).
46. R. S. Molina *et al.*, *In vivo* hypermutation and continuous evolution. *Nat. Rev. Methods Primers* **2**, e36 (2022).
47. S. J. Hendel, M. D. Shoulders, Directed evolution in mammalian cells. *Nat. Methods* **18**, 346–357 (2021).
48. O. Mueller-Cajar, M. Morell, S. M. Whitney, Directed evolution of Rubisco in *Escherichia coli* reveals a specificity-determining hydrogen bond in the Form II enzyme. *Biochem.* **46**, 14067–14074 (2007).
49. R. H. Wilson, S. M. Whitney, "Improving CO_2 fixation by enhancing Rubisco performance" in *Directed Enzyme Evolution: Advances and Applications*, M. Alcalde, Ed. (Springer International Publishing, 2017), pp. 101–126.
50. D. S. Kubien, C. M. Brown, H. J. Kane, Quantifying the amount and activity of Rubisco in leaves. *Methods Mol. Biol.* **684**, 349–362 (2010).
51. L. Whitehead, B. M. Long, G. D. Price, M. R. Badger, Comparing the *in vivo* function of α-carboxysomes and β-carboxysomes in two model cyanobacteria. *Plant Physiol.* **165**, 398–411 (2014).
52. H. Li, R. Durbin, Fast and accurate short read alignment with Burrows-Wheeler transform. *Bioinformatics* **25**, 1754–1760 (2009).
53. P. Danecek *et al.*, Twelve years of SAMtools and BCFtools. *Gigascience* **10**, giab008 (2021).
54. H. J. Kane *et al.*, An improved method for measuring the CO_2/O_2 specificity of Ribulosebisphosphate Carboxylase-Oxygenase. *Funct. Plant Biol.* **21**, 449 (1994).
55. S. M. Whitney, R. E. Sharwood, "Plastid transformation for Rubisco engineering and protocols for assessing expression" in *Chloroplast Biotechnology: Methods and Protocols* (Humana Press, 2014), pp. 245–262.
56. S. M. Whitney, P. Baldet, G. S. Hudson, T. J. Andrews, Form I Rubiscos from non-green algae are expressed abundantly but not assembled in tobacco chloroplasts. *Plant J.* **26**, 535–547 (2001).
57. M. D. Shoulders, In vivo directed evolution of an ultrafast Rubisco from a semianaerobic environment imparts oxygen resistance. NCBI. https://www.ncbi.nlm.nih.gov/bioproject/PRJNA1275035/. Deposited 11 June 2025.
58. J. L. McDonald *et al.*, Plasmids from "In vivo directed evolution of an ultrafast Rubisco from a semi-anaerobic environment imparts oxygen resistance." Addgene. https://www.addgene.org/browse/article/28253576/. Accessed 5 April 2025.